



OPEN

Tapered high-gain Fabry–Perot cavity antenna with high sidelobe suppression for 5G industry

Muhammad Hussain¹, Kyung-Geun Lee¹ & Dongho Kim²✉

We propose a Fabry–Perot cavity (FPC) antenna to suppress a sidelobe level (SLL) while maintaining a reasonably high gain. Generally, conventional FPC antennas (FPCAs) produce a high SLL because waves in their FPC leak considerably through lateral openings, which is a primary reason for lowering antenna gains. We propose two design approaches to solve this problem: the reflection magnitude tapering of a partially reflective surface (PRS) and considering different incident modes for the PRS design. First, the proposed tapering can remarkably reduce an SLL by providing the PRS with more radiation opportunities. Second, the different incident modes of transverse electric (TE) and transverse magnetic (TM) can increase an antenna gain by considering a more realistic illumination environment of the PRS. We have proven that our antenna provides 19.8 dBi realized gain with high sidelobe suppression (SLS) of more than 23 dB. Consequently, the proposed FPCA can suppress sidelobes significantly while maintaining a high gain. Good agreement between simulations and experiments demonstrates the usefulness of our proposal.

Conventional array antennas have been found in many practical applications^{1–7} due to their directional radiation patterns and versatile beamforming ability. Generally, these antennas have massive and complex feed structures^{8–10}, which induce unwanted power loss. Moreover, they also suffer from high sidelobes, which is an important index for many applications such as the 5G industry^{11–14}, urban air mobility (UAM), radar systems¹⁵, and wireless power transfer^{16,17}.

Transmitarrays¹⁸, reflectarrays^{19,20}, and resonance cavity antennas^{21,22} have been widely explored to overcome these problems, which also include power pattern reconfigurability^{20,21}. However, high sidelobes are still an obstacle for many applications.

To improve the gain and sidelobe suppression (SLS) properties of FPCAs, several PRS superstrates—a single-layer PRS^{23,24}, an inhomogeneous gradient-index PRS²⁵, and a multilayered PRS with different permittivity²⁶, a phased gradient surface²⁷, a phase correction structure²⁸, a double-layer nonuniform superstrate²⁹, an FPC with side walls³⁰—have been proposed. However, for the required properties, the PRSs are too complex to be engineered with a standard PCB process; even with them, the SLS performance is still not satisfactory.

To solve these problems, we propose a novel FPCA with a tapered PRS to maximally suppress side lobes with a reasonably high antenna gain. The tapered PRS provides gradually decreasing reflection magnitudes, which helps reduce undesirable energy leakage through lateral openings.

We newly introduce artificial magnetic conductors (AMC) cells to a reflectarray ground plane to minimize the expected gain reduction, which is designed to enforce Trentini's resonance condition in the cavity with corresponding tapered PRS cells³¹. All simulations were conducted using CST Studio Suite³².

Design and operation

The design model of the proposed FPCA is depicted in Fig. 1, which consists of a tapered PRS superstrate, a reflectarray, and an *x*-polarized aperture-coupled stacked microstrip patch antenna at the center of the FPCA. Here, a transmission line runs under the reflectarray to transfer electromagnetic energy to the stack patches through the slot. The reflectarray and transmission line substrates are firmly bonded by a 0.04 mm epoxy FR4 layer with relative permittivity (ϵ_r) = 4.3 and loss tangent ($\tan \delta$) = 0.025³³. A 1.52 mm thick Taconic RF-35 substrate is used to fabricate the FPCA, which has ϵ_r = 3.5 and $\tan \delta$ = 0.0025. Additionally, to minimize unwanted back radiation (in the *-z*-direction)³⁴, we intentionally install the reflector at optimum height h_2 , which also largely affects the impedance matching of our antenna³⁵.

¹Network Research Lab (NRL), Department of Information and Communication Engineering, Sejong University, Seoul 05006, Republic of Korea. ²Antenna and RF Applications Lab (ARFAL), Department of Electrical Engineering, Sejong University, Seoul 05006, Republic of Korea. ✉email: dongkim@sejong.ac.kr

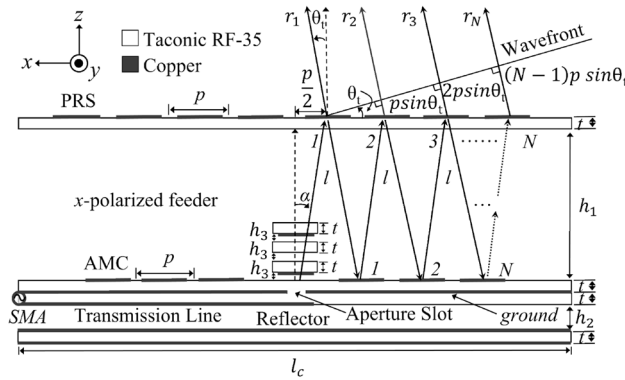


Figure 1. Operational principle of the proposed FPCA with $\alpha = \tan^{-1}(p/2h_1) = 26.6^\circ$, $l = h_1/\cos\alpha = 33.54$ mm, $h_1 = 0.52\lambda_0 = 31.6$ mm, $h_2 = 10$ mm, $h_3 = 0.5$ mm, $\lambda_0 = 60$ mm (at $f_0 = 5$ GHz), $l_c = 4.33\lambda_0 = 260$ mm, $p = 0.5\lambda_0 = 30$ mm, $t = 1.52$ mm, $\theta_t = 0^\circ$ (broadside direction), $N = 4$ for PRS unit cells and $N = 3$ for AMC unit cells.

Operation of the FPCA

The operational principle of the proposed FPCA is depicted in Fig. 1, providing a constructively built wavefront toward the target direction (θ_t). As well known, to obtain a high gain in the broadside direction, all the rays need to satisfy Trentini's resonance condition³¹, which is written as

$$\phi_{\Gamma_n}^{PRS} - 2\beta h_1 - \pi = \pm 2N\pi \quad (1)$$

where $\beta = 2\pi/\lambda_0$ is the free space phase constant, λ_0 is a wavelength in free space at design frequency (f_0) 5 GHz, and h_1 is the cavity height. $\phi_{\Gamma_n}^{PRS}$ is the reflection phase of the uniform PRS. N and n are the total and the n^{th} number of unit cells, respectively.

Conventional FPCAs consist of a uniform PRS and a metallic ground plane. Hence, we do not need to consider the transmission behavior of the PRS to derive FP resonance because all the PRS cells provide the same transmission phase. That is why we do not include the transmission property in (1).

However, when a PRS is tapered as ours, each cell exhibits different reflection and transmission properties, which does not satisfy the required FP resonance condition with a fixed cavity height. In addition, as we know, it is pretty tricky to control the reflection and transmission phase of the PRS unit cell independently. It is even more challenging with a single-layer PRS providing only limited reflection phase coverage.

To overcome this problem, we devise a reflectarray ground plane consisting of AMC unit cells to provide a desirable wide-enough reflection phase range. Consequently, we can form a highly-directive main beam satisfying the FP resonance condition with the help of the AMC cells. For the PRS and the AMC cell distribution in Fig. 1, following the ray from the source gives corresponding phase delays written as

$$\varphi_1 = -\beta l + \phi_{T1}^{PRS} \quad (2)$$

$$\varphi_2 = -3\beta l + \phi_{\Gamma1}^{PRS} + \phi_{\Gamma1}^{AMC} + \phi_{T2}^{PRS} - \beta p \sin \theta_t \quad (3)$$

$$\varphi_3 = -5\beta l + \phi_{\Gamma1}^{PRS} + \phi_{\Gamma1}^{AMC} + \phi_{\Gamma2}^{PRS} + \phi_{\Gamma2}^{AMC} + \phi_{T3}^{PRS} - 2\beta p \sin \theta_t \quad (4)$$

$$\varphi_n = -(2n-1)\beta l + \phi_{\Gamma1}^{PRS} + \phi_{\Gamma1}^{AMC} + \phi_{\Gamma2}^{PRS} + \phi_{\Gamma2}^{AMC} + \dots + \phi_{Tn}^{PRS} - (n-1)\beta p \sin \theta_t \quad (5)$$

Here, φ_n is the phase delay of the n^{th} ray r_n in Fig. 1 on the wavefront. All the phase delays ($\varphi_1, \varphi_2, \varphi_3, \dots, \varphi_n$) should be equal on the wavefront to produce intensive radiation at the target angle θ_t . Its rigorous derivation is provided in the Supplementary Section 1 "The rigorous derivation of the overall phase delay within the cavity". Comparing each phase delay from (2) to (5) yields

$$\phi_{\Gamma_n}^{AMC} = 2\beta l - \phi_{\Gamma_n}^{PRS} + \phi_{Tn}^{PRS} - \phi_{T_{n+1}}^{PRS} + \beta p \sin \theta_t \quad (6)$$

where $l = h_1/\cos\alpha$. The $\phi_{\Gamma_n}^{PRS}$ and ϕ_{Tn}^{PRS} are the reflection and transmission phases of the n^{th} PRS cell, and $\phi_{\Gamma_n}^{AMC}$ is the reflection phase of the n^{th} AMC cell. Therefore, we can confirm that introducing AMC cells makes it easier to enforce constructive interference in any target direction.

Reflection magnitude tapering of the PRS superstrate

The remarkably enhanced SLS is one of the essential goals of this work. So, we apply triangular tapering providing both high SLS and gain to the reflection magnitude of PRS cells³⁶, which is shown in Fig. 2 and written as

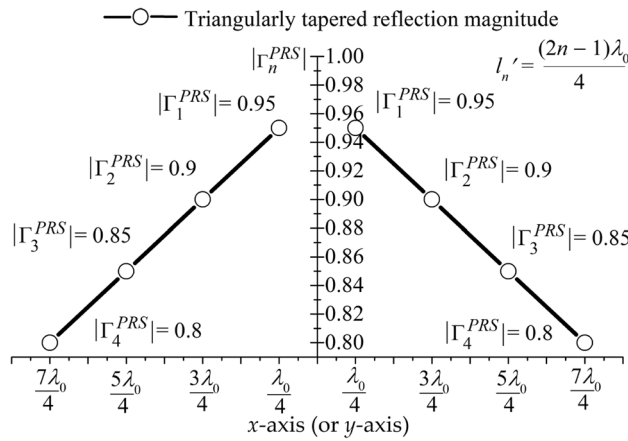


Figure 2. Triangular tapering applied to the reflection magnitude of the PRS.

$$|\Gamma_n^{PRS}| = |\Gamma_{min}^{PRS}| + |\Gamma_{OTR}^{PRS}| \left(1 - \frac{2}{l_c} |l_n'|\right) \tag{7}$$

Here, $|\Gamma_n^{PRS}|$ is the reflection magnitude of the n th PRS unit cell, $l_n' = (2n - 1)\lambda_0/4$, and $l_c = 4.3\lambda_0$ is a physical aperture length of the FPCA. $|\Gamma_{OTR}^{PRS}| = |\Gamma_{max}^{PRS}| - |\Gamma_{min}^{PRS}|$ is the tapered reflection magnitude range of the PRS. After intensive simulations, we tapered the reflection magnitude of the PRS cell to $0.8 \leq |\Gamma_n^{PRS}| \leq 0.95$.

The overall geometry of the proposed FPCA is illustrated in Fig. 3. Here, we will intentionally try three different tapering methods to analyze the effect of them: TE tapering (Fig. 3a), TM tapering [90° rotated version of Fig. 3a except the feeder], and full TE-TM tapering (Fig. 3b).

Considering that we use the x -polarized source feeder, incidence along the x - and y -axis becomes TM and TE modes, respectively, as shown in Fig. 4. Here, the incidence angle ($\alpha = \tan^{-1}(p/2h_1)$, in Fig. 1) is fixed at 26.6°.

In Fig. 3a, we expect highly suppressed sidelobes along the y -axis because we applied the TE tapering along the axis ($\phi = 90^\circ$). The deployment of the unit cells is described in detail in Supplementary Section 2 "PRS and AMC unit cells deployment for 1-D TE or TM tapering". Similarly, we can readily change Fig. 3a to TM tapering just by rotating the whole structure by 90° except for the feeding part.

Until now, we have demonstrated one-dimensional (1-D) tapering, i.e., TE or TM tapering along only one axis. However, it is worth trying tapering along both the x - and y -axes simultaneously for higher SLS, which is named 2-D (full TE-TM) tapering hereafter. In Fig. 3b, the 2-D tapering is applied to the PRS according to TE and TM incidences (see Fig. 4).

Design of the feeder, the PRS, and the reflectarray

Figure 5 depicts the geometry of the source feeder, consisting of two metal layers (as shown in Fig. 1). For better impedance matching, the transmission line is terminated with a cross-shape stub optimized through simulation.

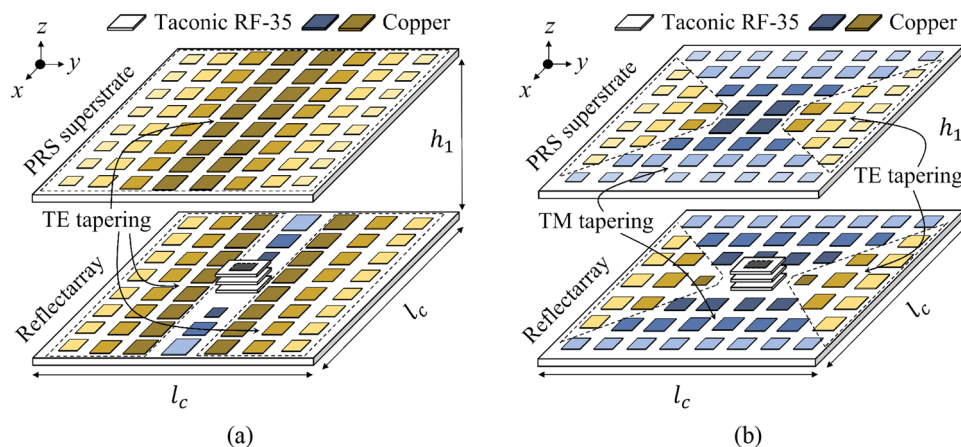


Figure 3. The FPCA models illustrate the proposed (a) 1-D TE tapering and (b) 2-D full TE-TM tapering.

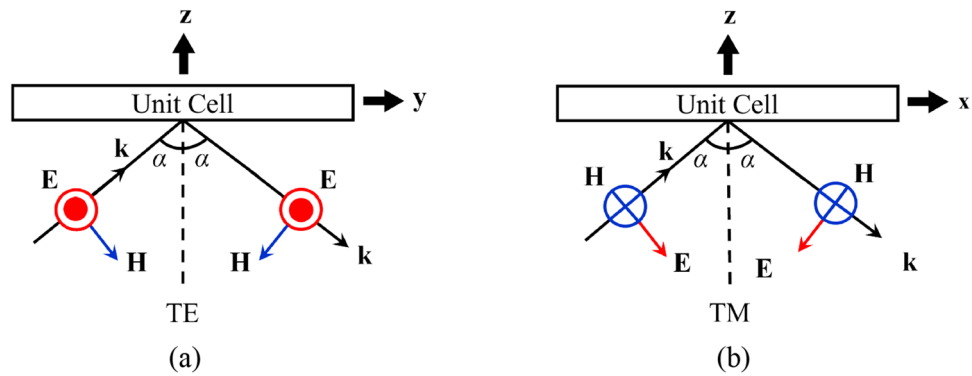


Figure 4. Two distinct incidence modes used for PRS and AMC unit cell simulations: (a) a TE mode and, (b) a TM mode with an incidence angle α .

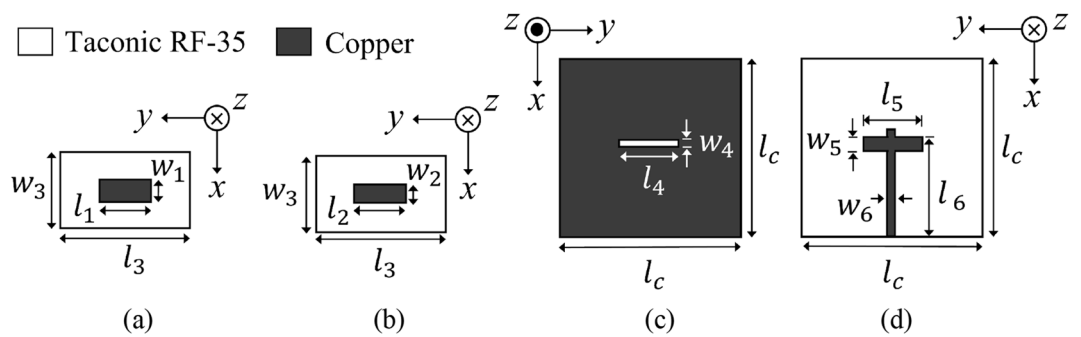


Figure 5. Exploded view of the source feeder: (a) 1st patch layer, (b) 2nd patch layer, (c) aperture slot layer, (d) transmission line layer with $l_1 = l_2 = 18.5$ mm, $l_3 = 37$ mm, $l_4 = 12.5$ mm, $l_5 = 13$ mm, $l_6 = 132.92$ mm, $l_c = 260$ mm, $w_1 = 14.53$ mm, $w_2 = 10.5$ mm, $w_3 = 29.06$ mm, $w_4 = 1.85$ mm, $w_5 = 5$ mm, $w_6 = 3.46$ mm [for 50 Ω impedance matching of a coaxial cable].

The reflection coefficient and the 3D radiation power pattern of the feeder are shown in the Supplementary Figs. S1 and S2, respectively.

The geometry of the PRS and AMC unit cells are also illustrated in Fig. 6. Each cell comprises a square metal patch on a Taconic RF-35 substrate. Only the bottom side of the AMC is fully covered with copper. The PRS and the AMC unit cells are designed to provide their reflection magnitudes in the ranges of $0.8 < |\Gamma_n^{PRS}| < 0.95$ and $0.81 < |\Gamma_n^{AMC}| < 1$, respectively.

The reflection and transmission characteristics of the PRS and AMC unit cells are illustrated in Fig. 7. The cells exhibit distinct behaviors under different incidences (see Fig. 4), which demonstrates why we need to consider the TE and TM incidence separately in our antenna design. As we can see the reflection phases, the AMC cells provides significantly larger phase range (see Fig. 7d) than the PRS, which is favorable to construct the cavity resonance condition and advantageous for the highly-directive beamforming in the targeted direction.

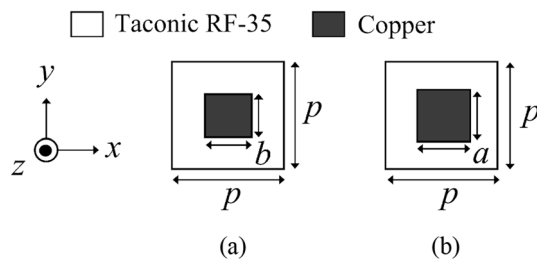


Figure 6. The geometry of a (a) PRS unit cell with $p = 30$ mm, $b = 14 \sim 26$ mm; and an (b) AMC unit cell with $a = 10 \sim 28$ mm.

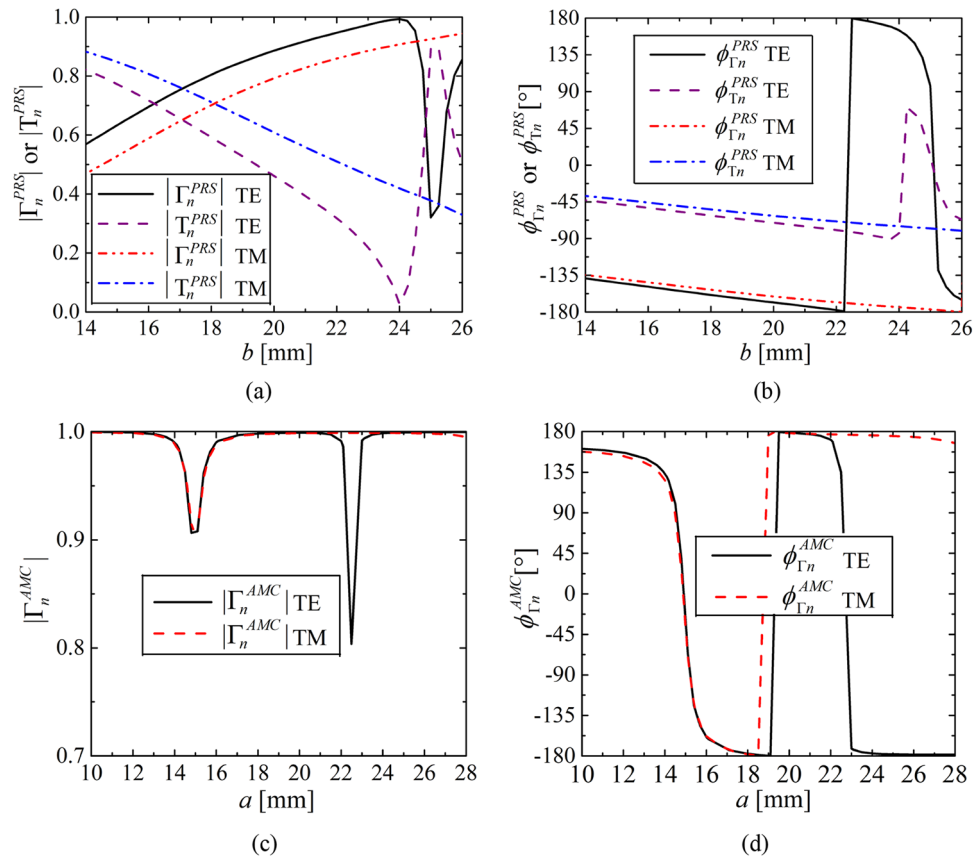


Figure 7. Reflection and transmission coefficients of both PRS and AMC cells (see Fig. 6) reveal distinct behaviors under TE and TM incidence that’s why we considered both incidences separately for the proposed TE and TM tapering at 5 GHz: (a) reflection $|\Gamma_n^{PRS}|$ and transmission $|\Gamma_n^{PRS}|$ magnitudes of the PRS, (b) reflection $\phi_{\Gamma_n}^{PRS}$ and transmission $\phi_{\Gamma_n}^{PRS}$ phases of the PRS, (c) reflection magnitude $|\Gamma_n^{AMC}|$ of the AMC, and (d) reflection phase $\phi_{\Gamma_n}^{AMC}$ of the AMC.

| Values | $n=1$ | $n=2$ | $n=3$ | $n=4$ |
|-------------------------|---------------|---------------|--------------|------------------|
| $ \Gamma_n^{PRS} $ | 0.95 | 0.9 | 0.85 | 0.8 |
| $ \Gamma_n^{PRS} $ | 0.3 | 0.43 | 0.52 | 0.59 |
| $\phi_{\Gamma_n}^{PRS}$ | -180° | -173° | -167° | -161.5° |
| $\phi_{\Gamma_n}^{PRS}$ | -80.5° | -74° | -68° | -63° |
| b | 26 mm | 23.65 mm | 21.68 mm | 20.2 mm |
| $\phi_{\Gamma_n}^{AMC}$ | -176° | 177.5° | 173° | N/A ¹ |
| a | 17.55 mm | 20.74 mm | 26.43 mm | N/A |

Table 1. The reflection and transmission properties of the PRS superstrate and the reflectarray for TE incidence. ¹N/A stands for not available.

The optimized magnitude and phase characteristics of the tapered PRS and the reflectarray are listed in Tables 1 and 2 under TE and TM incidences, respectively. Here, the high reflection magnitude of the PRS, $0.8 < |\Gamma_n^{PRS}| < 0.95$, and the AMC, $0.81 < |\Gamma_n^{AMC}| < 1$ are desirable for high SLS and maximizing realized gain.

Simulation and experiment results 1-D (TE or TM) tapering

The impedance matching behavior and radiation patterns of the FPCA with 1-D (TE and TM) tapering are simulated and given in Figs. 8 and 9. The -10 dB impedance bandwidth is well maintained around the design frequency of 5 GHz. Here, the TE tapering provides a broader bandwidth because AMC cells adjacent to the feeder behave differently for TE and TM design. As for the maximum realized gain, the TM tapering gives a

| Values | $n=1$ | $n=2$ | $n=3$ | $n=4$ |
|-------------------------|--------------|---------------|---------------|----------------|
| $ \Gamma_n^{PRS} $ | 0.95 | 0.9 | 0.85 | 0.8 |
| $ \Gamma_n^{PRS} $ | 0.3 | 0.43 | 0.52 | 0.59 |
| $\phi_{\Gamma_n^{PRS}}$ | -178° | -170° | -164° | -158.5° |
| $\phi_{\Gamma_n^{PRS}}$ | -80° | -72.5° | -66.5° | -61.5° |
| b | 22.14 mm | 20.42 mm | 19.04 mm | 17.91 mm |
| $\phi_{\Gamma_n^{AMC}}$ | -179° | 174.5° | 169.5° | N/A |
| a | 18.62 mm | 21.58 mm | 22.05 mm | N/A |

Table 2. The reflection and transmission properties of the PRS superstrate and the reflectarray for TM incidence.

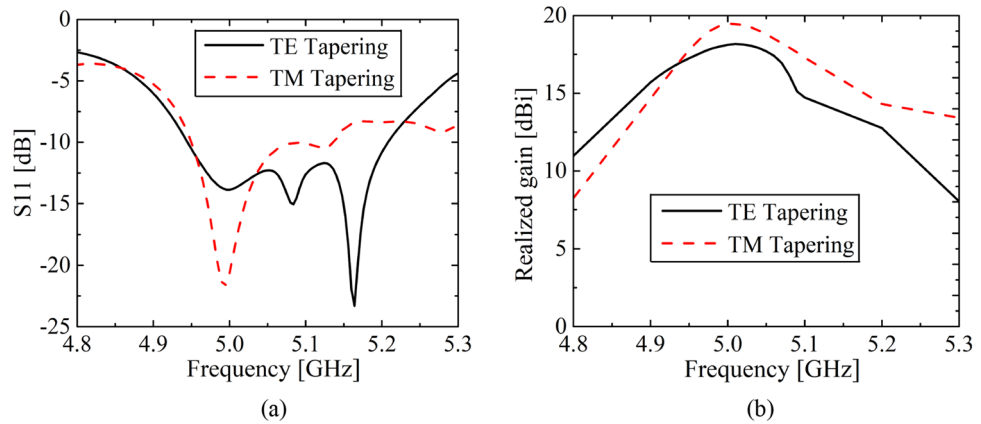


Figure 8. (a) Antenna reflection coefficient S11 and (b) peak realized gain of the 1-D TE tapering and 1-D TM tapering.

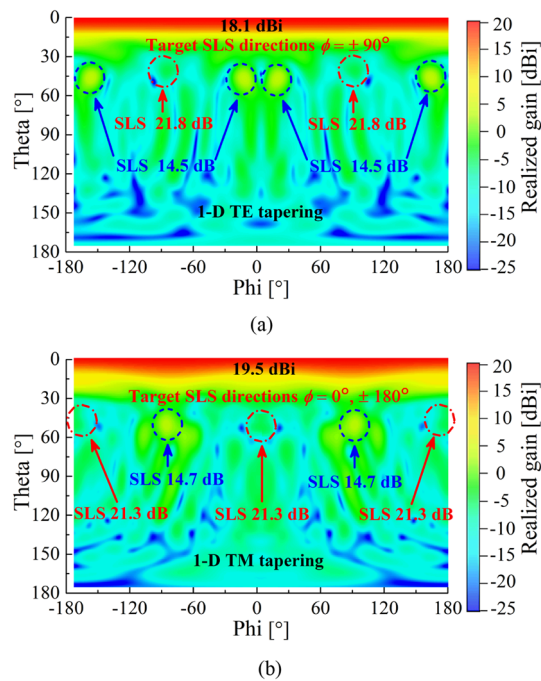


Figure 9. Radiation patterns (realized gain) after applying (a) 1-D TE tapering and (b) 1-D TM tapering to the y - ($\phi = \pm 90^\circ$) and x -axis ($\phi = 0^\circ$ and 180°), respectively. Both are simulated at 5 GHz.

higher gain around 5 GHz, as presented in Fig. 8b. For both cases, a gradual reduction of the gains at lower and higher frequencies is because of increasing deviation from FPC resonance and poor impedance matching.

The primary objective of the 1-D (TE or TM) tapering is to obtain high SLS along the corresponding tapering axis, with minimum reduction in an antenna gain. After applying the 1-D (TE or TM) tapering, radiation power patterns are illustrated in Fig. 9 to validate how much the SLS is enhanced. For the 1-D TE tapering applied along the y -axis, we expect high SLS along the axis ($\phi = \pm 90^\circ$), which is confirmed by high 21.8 dB SLS at $\phi = \pm 90^\circ$ in Fig. 9a. Considering the relatively low SLS of 14.5 dB observed at $\phi = \pm 15^\circ$ and $\pm 165^\circ$ implies our tapering method is effective only around the tapering direction. Similarly, we can prove from Fig. 9b that the 1-D TM tapering also increases the SLS up to 21.3 dB in the directions ($\phi = 0^\circ$ and 180°) where the tapering is applied. Again, the 14.7 dB SLS at $\phi = \pm 90^\circ$ validates that tapering is effective only around the tapering-applied axis. The peak gains of the two tapering cases are 18.1 dBi (TE) and 19.5 dBi (TM), respectively. The 3D radiation patterns of the 1-D (TE or TM) tapering are illustrated in the Supplementary Figs. S3 and S4, respectively.

2-D (full TE-TM) tapering

We move on to the 2-D (full TE-TM) tapering, which combines the 1-D TE and TM tapering, according to the way illustrated in Fig. 3b. Figure 10 shows a radiation pattern after applying the 2-D tapering. Here, we can find high SLS levels of 25 dB and 23.3 dB along the x - ($\phi = 0^\circ$ and 180° , E-plane) and y - ($\phi = \pm 90^\circ$, H-plane) axis, respectively. Therefore, we can say that the proposed tapering method obviously helps suppress sidelobes even with no reflective side walls. It is also worth that the tapering increases the peak gain up to 19.8 dBi. The 3D radiation pattern of the 2-D (full TE-TM) tapering is illustrated in the Supplementary Fig. S5.

To check the validity of our design in terms of 3-D field distribution, we pick up the magnitude and the phase distributions of the dominant E_x -field 30 mm above the PRS, which is given in Fig. 11. The square with dotted lines is a footprint of the PRS. Both distributions change little around the x - and y -axis, which implies the antenna satisfies the FPC resonance condition very well. However, they vary more significantly in the diagonal directions, so there is still room for further SLS in the diagonal cell design, which is a future research topic.

The fabricated antenna is shown in Fig. 12, which consists of 64 PRS and 54 AMC cells measuring 260 mm ($4.3 \lambda_0$) \times 260 mm ($4.3 \lambda_0$) \times 31.6 mm ($0.52 \lambda_0$). The FPCA is very sensitive to cavity height, so we used 20 plastic M4 spacers to keep the PRS as flat as possible.

The impedance matching and the peak realized gain behaviors of the FPCA with and without 2-D tapering applied PRS are given in Fig. 13. The measured -10 dB impedance bandwidth is about 187 MHz, corresponding to 3.7% fractional bandwidth, which follows the simulation relatively well. The impedance measurement setup

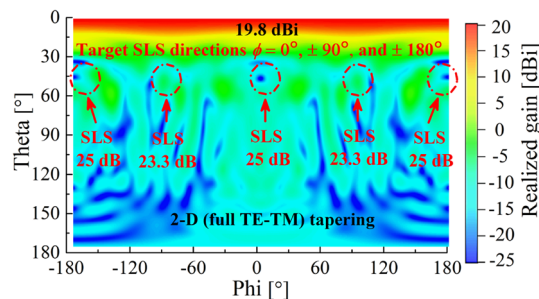


Figure 10. Radiation patterns (realized gain) after applying 2-D (full TE-TM) tapering at 5 GHz.

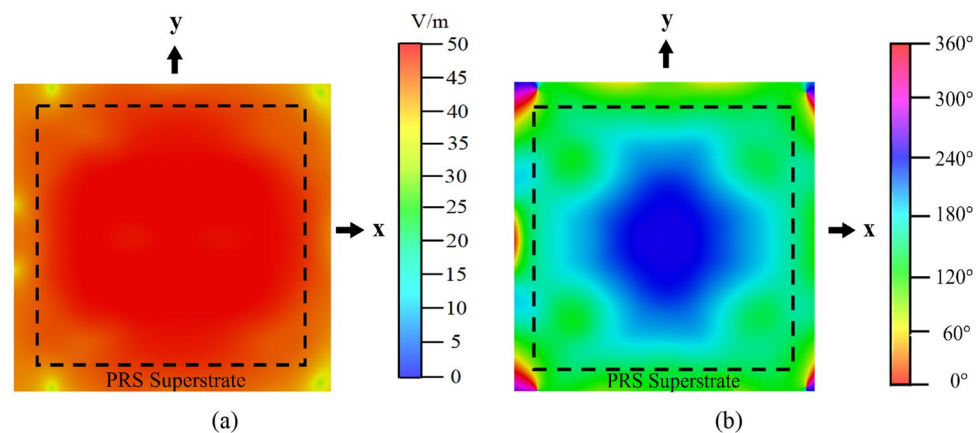


Figure 11. E_x -field (a) magnitude and (b) phase distribution at 30 mm above the 2-D tapered PRS superstrate at 5 GHz.

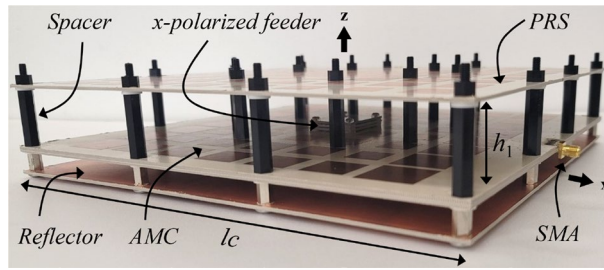


Figure 12. Fabricated FPCA with 20 plastic M4 spacers.

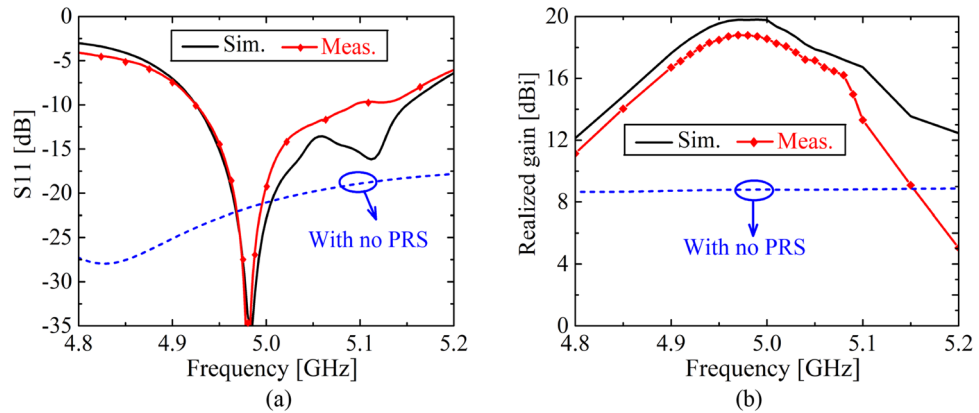


Figure 13. (a) Antenna reflection coefficient S_{11} , and (b) peak realized gain of the FPCA with and without the 2-D (full TE-TM) tapering applied PRS.

is shown in the Supplementary Fig. S6. As for the maximum realized gain, the measured peak gain is 18.8 dBi, which is 1 dB lower than the simulation. The deviation between the gains is greater at higher frequencies because the PRS is not completely flat, which is a common problem resulting from a chemical etching process. In this work, we used 20 spacers to keep the PRS as flat as possible, but in the end, we could not make it perfectly flat. That explains the large gain deviation in higher frequencies.

The radiation patterns of the FPCA with and without 2-D tapering applied PRS are also given in Fig. 14. The measured radiation pattern of the FPCA is done in an echoic chamber, which is depicted in the Supplementary Figs. S7 and S8, respectively. We can see that sidelobes on both the E- ($\phi = 0^\circ$ and 180° , x -axis) and H-planes

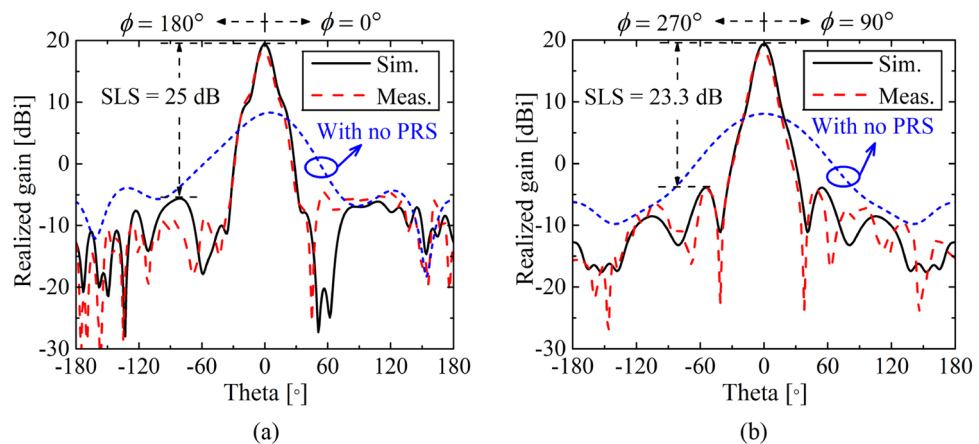


Figure 14. Radiation patterns (realized gain) along (a) x -axis ($\phi = 0^\circ$ & 180° , E-plane) and (b) y -axis ($\phi = \pm 90^\circ$, H-plane) of the 2-D (full TE-TM) tapering of the FPCA with and without PRS at the $f_0 = 5$ GHz. Here, sidelobes are well suppressed below 23.3 dB on both E- and H-planes thanks to a proposed 2-D tapering method.

| Antenna performance | Tapering method | | | |
|---|-----------------|----------|-------------|-------------|
| | Simulation | | | Measured |
| | 1-D (TE) | 1-D (TM) | 2-D (TE-TM) | 2-D (TE-TM) |
| Impedance bandwidth ¹ | 263 MHz | 187 MHz | 236 MHz | 186 MHz |
| Fractional bandwidth | 5.1 % | 3.7 % | 4.5 % | 3.7 % |
| Realized gain | 18.1 dBi | 19.5 dBi | 19.8 dBi | 18.8 dBi |
| Radiation efficiency | 90 % | 90 % | 91 % | 91 % |
| Total efficiency | 87 % | 89 % | 90 % | 90 % |
| Aperture efficiency | 28 % | 38 % | 41 % | 35 % |
| SLS (x -axis, $\phi = 0^\circ$ & 180°) | 14.5 dB | 21.3 dB | 25 dB | 23.5 dB |
| SLS (y -axis, $\phi = \pm 90^\circ$) | 21.8 dB | 14.7 dB | 23.3 dB | 23.3 dB |

Table 3. Antenna performance variation according to the tapering methods. ¹Measured at $S_{11} = -10$ dB.

| Refs. | f_0 (GHz) | FBW ¹ (%) | No. of PRS layers | PRS thickness (mm) | Aperture area (λ_0^2) | Antenna height (λ_0) | Realized gain (dBi) | Aperture efficiency (%) | SLS (dB) x -axis, $\phi = 0^\circ$ and 180° | SLS (dB) y -axis, $\phi = \pm 90^\circ$ |
|---------------|-------------|----------------------|-------------------|--------------------|---------------------------------|--------------------------------|---------------------|-------------------------|--|---|
| ²³ | 61.4 | 14.8 | 1 | 1.27 | 10.09 | 0.47 | 11.00 | 9.9 | 4.5 | 15.4 |
| ²⁴ | 13.5 | 14.4 | 1 | 1.575 | 10.24 | 0.60 | 17.90 | 47.9 | 10.0 | 11.0 |
| ²⁵ | 7.0 | N/A ² | 1 | 5.08 | 3.14 | 0.50 | 14.03 | 64.0 | 14.9 | 14.9 |
| ²⁶ | 10.0 | 30.0 | 3 | 23.30 | 4.00 | 1.34 | 17.40 | 27.3 | 9.0 | 12.0 |
| ²⁷ | 5.36 | 3.5 | 1 | 1.578 | 4.29 | 0.10 | 9.12 | 15.14 | 9.0 | 10.0 |
| ²⁸ | 5.8 | 1.4 | 2 | 7.00 | 11.76 | 0.52 | 20.78 | 80.9 | 20.0 | 20.0 |
| ²⁹ | 5.8 | 4.7 | 2 | 17.00 | 9.62 | 0.68 | 19.40 | 72.0 | 17.0 | 17.0 |
| This work | 5.0 | 5.1 | 1 | 1.52 | 18.75 | 0.52 | 19.80 | 40.5 | 25.0 | 23.3 |

Table 4. Antenna performance comparison with previous FPCAs. ¹Fractional bandwidth, ²N/A stand for not available.

($\phi = 90^\circ$ and 270° , y -axis) are suppressed well below 23.3 dB thanks to the proposed 2-D tapering method. Half power beam widths are 14.4° and 16.4° on the E- and H-planes, respectively. The sidelobe suppression along $\phi = 45^\circ$ and 225° is depicted in Supplementary Fig. S9.

Our antenna suppresses side lobes the best with a reasonably high antenna gain and aperture efficiency. Some important antenna performance according to the applied tapering methods is summarized in Table 3. Our work is also compared with recently published related works in Table 4.

Conclusion

In this work, we have proposed a novel FPCA to improve SLS property while maintaining a high antenna gain. We have applied the 1-D and 2-D tapering to the reflection magnitude of the PRS to suppress the sidelobes. Moreover, we have used additional AMC cells along with the PRS to make the FPC satisfy Trentini's resonance, which helps maintain a reasonably high gain.

Accordingly, our FPCA has attained more than 23 dB high SLS with a peak realized gain of 19.8 dBi.

The proposed FPCA has a simple configuration but simultaneously provides a relatively high gain and SLS. Therefore, we expect our antenna to find many potential applications requiring a high gain and SLS, such as 5G communications, radars, satellite systems, and urban air mobility (UAM).

Data availability

All data required to evaluate the findings of this work is available in the presented paper. Additional data related to this work may be requested from the corresponding author.

Received: 2 June 2023; Accepted: 14 September 2023

Published online: 21 September 2023

References

- Shen, F., Mu, J., Guo, K., Wang, S. & Guo, Z. Generation of continuously variable-mode vortex electromagnetic waves with three-dimensional helical antenna. *IEEE Antennas Wirel. Propag. Lett.* **18**(6), 1091–1095 (2019).
- Garufo, A., Llobart, N. & Neto, A. Radiation of logarithmic spiral antennas in the presence of dense dielectric lenses. *IEEE Trans. Antennas Propag.* **64**(10), 4168–4177 (2016).
- Mahajan, M., Jyoti, R., Sood, K. & Sharma, S. B. A method of generating simultaneous contoured and pencil beams from single shaped reflector antenna. *IEEE Trans. Antennas Propag.* **61**(10), 5297–5301 (2013).
- Marinović, T. *et al.* Fast characterization of mutually coupled array antennas using isolated antenna far-field data. *IEEE Trans. Antennas Propag.* **69**(1), 206–218 (2020).

5. Zhang, Y. X., Jiao, Y. C. & Zhang, L. Wideband circularly polarized array antennas with sequential-rotation polarization grid and simplified full-SIW feeding networks. *IEEE Trans. Antennas Propag.* **68**(8), 6088–6097 (2020).
6. Park, J. D., Rahman, M. & Chen, H. N. Isolation enhancement of wide-band MIMO array antennas utilizing resistive loading. *IEEE Access* **7**, 81020–81026 (2019).
7. Kittiyapunya, C. & Krairiksh, M. A four-beam pattern reconfigurable Yagi-Uda antenna. *IEEE Trans. Antennas Propag.* **61**(12), 6210–6214 (2013).
8. Yang, G., Li, J., Wei, D. & Xu, R. Study on wide-angle scanning linear phased array antenna. *IEEE Trans. Antennas Propag.* **66**(1), 450–455 (2018).
9. Kim, S. & Nam, S. A compact and wideband linear array antenna with low mutual coupling. *IEEE Trans. Antennas Propag.* **67**(8), 5695–5699 (2019).
10. Yang, H., Cao, X., Gao, J., Yang, H. & Li, T. A wide-beam antenna for wide-angle scanning linear phased arrays. *IEEE Antennas Wirel. Propag. Lett.* **19**(12), 2122–2126 (2020).
11. Khalid, M. *et al.* 4-port MIMO antenna with defected ground structure for 5G millimeter wave applications. *Electronics* **9**(1), 71 (2020).
12. Park, S. J. & Park, S. O. LHCP and RHCP substrate integrated waveguide antenna arrays for millimeter-wave applications. *IEEE Antennas Wirel. Propag. Lett.* **16**, 601–604 (2016).
13. Huang, G. C., Iskander, M. F., Hoque, M., Goodall, S. R. & Bocskor, T. Antenna array design and system for directional networking. *IEEE Antennas Wirel. Propag. Lett.* **14**, 1141–1144 (2015).
14. Hussain, M., Amin, Y. & Lee, K.-G. A compact and flexible UHF RFID tag antenna for massive IoT devices in 5G system. *Sensors* **20**(19), 5713 (2020).
15. Mirmozafari, M. & Zhang, G. On sidelobe problem of configured array antennas. *IEEE Trans. Antennas Propag.* **66**(7), 3475–3481 (2018).
16. Shen, G. *et al.* Suppressing sidelobe level of the planar antenna array in wireless power transmission. *IEEE Access* **7**, 6958–6970 (2019).
17. Park, I., Seo, C. & Ku, H. Sidelobe suppression beamforming using tapered amplitude distribution for a microwave power transfer system with a planar array antenna. *J. Electromagn. Eng. Sci.* **22**(1), 64–73 (2022).
18. Hasani, H., Silva, J. S., Capdevila, S., García-Vigueras, M. & Mosig, J. R. Dual-band circularly polarized transmitarray antenna for satellite communications at (20, 30) GHz. *IEEE Trans. Antennas Propag.* **67**(8), 5325–5333 (2019).
19. Deng, R., Xu, S., Yang, F. & Li, M. Single-layer dual-band reflectarray antennas with wide frequency ratios and high aperture efficiencies using phoenix elements. *IEEE Trans. Antennas Propag.* **65**(2), 612–622 (2017).
20. Nam, I. J., Lee, S. & Kim, D. Miniaturized beam reconfigurable reflectarray antenna with wide 3-D beam coverage. *IEEE Trans. Antennas Propag.* **70**(4), 2613–2622 (2022).
21. Jang, W., Jeon, Y. G., Maeng, H. J., Kim, J. & Kim, D. Novel beam scan method of Fabry-Perot Cavity (FPC) antennas. *Appl. Sci.* **11**(22), 11005 (2021).
22. Rabbani, M. S., Churm, J. & Feresidis, A. P. continuous beam-steering low-loss millimeter-wave antenna based on a piezo-electrically actuated metasurface. *IEEE Trans. Antennas Propag.* **70**(4), 2439–2449 (2021).
23. Almutawa, A. T., Hosseini, A., Jackson, D. R. & Capolino, F. Leaky-wave analysis of wideband planar Fabry-Pérot cavity antennas formed by a thick PRS. *IEEE Trans. Antennas Propag.* **67**(8), 5163–5175 (2019).
24. Liu, Z. G., Lu, W. B. & Yang, W. Enhanced bandwidth of high directive emission Fabry-Perot resonator antenna with tapered near-zero effective index using metasurface. *Sci. Rep.* **7**(1), 11455 (2017).
25. Zaiter, S., Raveu, N. & Oussaid, R. A new inhomogeneous partially reflecting surface for Fabry-Perot antenna to reduce side lobe level. *Int. J. RF Microw. Comput. Aided Eng.* **30**(7), 22229 (2020).
26. Ponti, C., Baccarelli, P., Ceccuzzi, S. & Schettini, G. Tapered all-dielectric EBGs with 3-D additive manufacturing for high-gain resonant-cavity antennas. *IEEE Trans. Antennas Propag.* **69**(5), 2473–2480 (2020).
27. Illahi, M. U., Khan, M. U., Hussain, R. & Tahir, F. A. A highly compact Fabry Perot cavity-based MIMO antenna with decorrelated fields. *Sci. Rep.* **12**(1), 1–11 (2022).
28. Zhou, L., Duan, X., Luo, Z., Zhou, Y. & Chen, X. High directivity Fabry-Pérot antenna with a nonuniform partially reflective surface and a phase correcting structure. *IEEE Trans. Antennas Propag.* **68**(11), 7601–7606 (2020).
29. Zhou, L., Chen, X. & Duan, X. Fabry-Pérot resonator antenna with high aperture efficiency using a double-layer nonuniform superstrate. *IEEE Trans. Antennas Propag.* **66**(4), 2061–2066 (2018).
30. Lee, J. G. Compact and robust Fabry-Perot cavity antenna with PEC wall. *J. Electromagn. Eng. Sci.* **21**(3), 184–188 (2021).
31. Trentini, G. V. Partially reflecting sheet arrays. *IRE Trans. Antennas Propag.* **4**(4), 666–671 (1956).
32. CST Microwave Studio Suite. Available <http://www.cst.com/> (2023).
33. Hussain, M., Lee, K.-G. & Kim, D. Circularly polarized high-gain Fabry-Perot cavity antenna with high sidelobe suppression. *Appl. Sci.* **13**(14), 8222 (2023).
34. Rowe, W. S. T. & Waterhouse, R. B. Reduction of backward radiation for CPW fed aperture stacked patch antennas on small ground planes. *IEEE Trans. Antennas Propag.* **51**(6), 1411–1413 (2003).
35. Latif, S. I., & Shafai, L. Effects of reflector size and spacing on microstrip slot antenna performance. In *IEEE International Symposium on Antenna Technology and Applied Electromagnetic and URSI Conference*, 1–4 (2004).
36. Balanis, C. A. *Antenna Theory Analysis and Design* (A John Wiley & Sons. Inc., 2005).

Acknowledgements

This work was supported by the National Research Foundation of Korea (NRF) grant funded by the Korean government (Ministry of Science and ICT) under Grant NRF-2018R1D1A09082807 and NRF-2020R1A2C2013466.

Author contributions

M. H., K.-G. L. and D. K. were responsible for the experimental design and interpretation as well as writing and finalisation of the manuscript. All authors reviewed the manuscript.

Competing interests

The authors declare no competing interests.

Additional information

Supplementary Information The online version contains supplementary material available at <https://doi.org/10.1038/s41598-023-42716-8>.

Correspondence and requests for materials should be addressed to D.K.

Reprints and permissions information is available at www.nature.com/reprints.

Publisher's note Springer Nature remains neutral with regard to jurisdictional claims in published maps and institutional affiliations.



Open Access This article is licensed under a Creative Commons Attribution 4.0 International License, which permits use, sharing, adaptation, distribution and reproduction in any medium or format, as long as you give appropriate credit to the original author(s) and the source, provide a link to the Creative Commons licence, and indicate if changes were made. The images or other third party material in this article are included in the article's Creative Commons licence, unless indicated otherwise in a credit line to the material. If material is not included in the article's Creative Commons licence and your intended use is not permitted by statutory regulation or exceeds the permitted use, you will need to obtain permission directly from the copyright holder. To view a copy of this licence, visit <http://creativecommons.org/licenses/by/4.0/>.

© The Author(s) 2023